

The *K2* & *TESS* Synergy I: Updated Ephemerides and Parameters for K2-114, K2-167, K2-237, & K2-261

MMA IKWUT-UKWA ¹, JOSEPH E. RODRIGUEZ ¹, ALLYSON BIERYLA ¹, ANDREW VANDERBURG ^{2,*}, TEO MOCNIK ³,
STEPHEN R. KANE ³, SAMUEL N. QUINN ¹, KNICOLE D. COLÓN ^{4,5}, GEORGE ZHOU ^{1,†}, JASON D. EASTMAN ¹,
CHELSEA X. HUANG ^{6,‡}, DAVID W. LATHAM ¹, JESSIE DOTSON ⁷, JON M. JENKINS ⁷, GEORGE R. RICKER ⁶,
SARA SEAGER ^{6,8,9}, ROLAND K. VANDERSPEK ⁶, JOSHUA N. WINN ¹⁰, THOMAS BARCLAY ^{4,11,5}, GEERT BARENTSEN ⁷,
ZACHORY BERTA-THOMPSON ¹², DAVID CHARBONNEAU ¹, DIANA DRAGOMIR ¹³, TANSU DAYLAN ^{6,§},
MAXIMILIAN N. GÜNTHER ^{6,‡}, CHRISTINA HEDGES ⁷, CHRISTOPHER E. HENZE ⁷, SCOTT MCDERMOTT ¹⁴,
JOSHUA E. SCHLIEDER ^{4,5}, ELISA V. QUINTANA ^{4,5}, JEFFREY C. SMITH ^{15,7}, JOSEPH D. TWICKEN ^{15,7},
DANIEL A. YAHALOMI ¹

¹Center for Astrophysics | Harvard & Smithsonian, 60 Garden St, Cambridge, MA 02138, USA

²Department of Astronomy, The University of Texas at Austin, Austin, TX 78712, USA

³Department of Earth and Planetary Sciences, University of California, Riverside, CA 92521, USA

⁴Exoplanets and Stellar Astrophysics Laboratory, Code 667, NASA Goddard Space Flight Center, Greenbelt, MD 20771, USA

⁵GSFC Sellers Exoplanet Environments Collaboration, NASA Goddard Space Flight Center, Greenbelt, MD 20771, USA

⁶Department of Physics and Kavli Institute for Astrophysics and Space Research, Massachusetts Institute of Technology, Cambridge, MA 02139, USA

⁷NASA Ames Research Center, Moffett Field, CA, 94035, USA

⁸Department of Earth, Atmospheric and Planetary Sciences, Massachusetts Institute of Technology, Cambridge, MA 02139, USA

⁹Department of Aeronautics and Astronautics, MIT, 77 Massachusetts Avenue, Cambridge, MA 02139, USA

¹⁰Department of Astrophysical Sciences, Princeton University, 4 Ivy Lane, Princeton, NJ, 08544, USA

¹¹University of Maryland, Baltimore County, 1000 Hilltop Circle, Baltimore, MD 21250, USA

¹²Department of Astrophysical and Planetary Sciences, University of Colorado, Boulder, CO 80309, USA

¹³Department of Physics & Astronomy, University of New Mexico, 1919 Lomas Blvd NE, Albuquerque, NM 87131, USA

¹⁴Proto-Logic Consulting LLC, Washington, DC 20009, USA

¹⁵SETI Institute, Mountain View, CA 94043, USA

ABSTRACT

Although the *TESS* primary mission observed the northern and southern ecliptic hemispheres, generally avoiding the ecliptic, and the *Kepler* space telescope during the *K2* mission could only observe near the ecliptic, many of the *K2* fields extend far enough from the ecliptic plane that sections overlap with *TESS* fields. Using photometric observations from both *K2* and *TESS*, combined with archival spectroscopic observations, we globally modeled four known planetary systems discovered by *K2* that were observed in the first year of the primary *TESS* mission. Specifically, we provide updated ephemerides and system parameters for K2-114 b, K2-167 b, K2-237 b, and K2-261 b. These were some of the first *K2* planets to be observed by *TESS* in the first year and include three Jovian sized planets and a sub-Neptune with orbital periods less than 12 days. In each case, the updated ephemeris significantly reduces the uncertainty in prediction of future times of transit, which is valuable for planning observations with the James Webb Space Telescope and other future facilities. The *TESS* extended mission is expected to observe about half of the *K2* fields, providing the opportunity to perform this type of analysis on a larger number of systems.

1. INTRODUCTION

The upcoming generation of telescopes, including the James Webb Space Telescope (*JWST*, Gardner et al. 2006)

and the Extremely Large Telescopes (ELTs) with highly sensitive instrumentation (e.g. Szentgyorgyi et al. 2016), will revolutionize the study of exoplanets. These telescopes will enable high-precision follow-up observations of transiting exoplanets, including atmospheric characterization of small planets ($R_p < 4 R_{\oplus}$). Additionally, future missions are being planned with the hope of detecting biosignatures in the atmospheres of small planets (Roberge & Moustakas 2018; Gaudi et al. 2018). The targets for these new telescopes will be planets previously discovered by missions like NASA's *Kepler* (Borucki et al. 2010) and the Transiting Exoplanet Sur-

Corresponding author: Mma Ikwut-Ukwa

mma.ikwut-ukwa@cfa.harvard.edu

* NASA Sagan Fellow

† NASA Hubble Fellow

‡ Juan Carlos Torres Fellow

§ Kavli Fellow

Table 1. Literature Properties for K2-114, K2-167, K2-237, & K2-261

Parameter	Description	K2-114	K2-167	K2-237	K2-261	Source
Other identifiers		2MASS J08313191+1155202	HD 212657	2MASS J16550453-2842380	TYC 255-257-1	
		TOI-514	TOI-1407	TOI-1049	TOI-685	
		TIC 366576758	TIC 69747919	TIC 16288184	TIC 281731203	
		EPIC 211418729	EPIC 205904628	EPIC 229426032	EPIC 201498078	
α_{J2000}	Right Ascension (RA)	08:31:31.913	22:26:18.190	16:55:04.534	10:52:07.779	1
δ_{J2000}	Declination (Dec)	+11:55:20.156	-18:00:40.220	-28:42:38.0150	+00:29:36.086	1
l	Galactic Longitude	127.88291401°	336.576123339°	253.76884794°	163.03231188°	1
b	Galactic Latitude	11.92225517°	-18.01166503°	-28.71058359°	+00.49316696°	1
B_T	Tycho B_T mag.	—	8.879 ± 0.02	—	11.805±0.086	2
V_T	Tycho V_T mag.	—	8.301 ± 0.02	—	10.717±0.059	2
G	Gaia G mag.	14.2751±0.02	8.104±0.02	11.467±0.02	10.459±0.02	1
GBp	Gaia B_p mag.	14.806±0.02	8.401±0.02	11.776±0.02	10.872±0.02	1
GRp	Gaia R_p mag.	13.615±0.02	7.688±0.02	11.012±0.02	9.917±0.02	1
J	2MASS J mag.	12.835 ± 0.02	7.202±0.02	10.508±0.02	9.337±0.03	3
H	2MASS H mag.	12.386 ± 0.03	6.974±0.04	10.268±0.02	8.920±0.04	3
K_S	2MASS K_S mag.	12.304 ± 0.03	6.887±0.03	10.217±	8.890±0.02	3
$WISE1$	$WISE1$ mag.	9.213 ± 0.022	6.810±0.055	10.105 ^{0.03} _{0.023}	8.828 ^{0.03} _{0.023}	4
$WISE2$	$WISE2$ mag.	9.245 ± 0.02	6.866 ^{0.03} _{0.02}	10.129 ^{0.03} _{0.02}	8.897 ^{0.03} _{0.02}	4
$WISE3$	$WISE3$ mag.	—	6.906 ^{0.03} _{0.017}	9.972±0.077	8.819±0.031	4
$WISE4$	$WISE4$ mag.	—	6.917±0.1	—	—	4
μ_α	Gaia proper motion in RA (mas yr ⁻¹)	-13.149±0.061	73.606±0.105	-8.568±0.100	-23.664±0.075	1
μ_δ	Gaia proper motion in DEC (mas yr ⁻¹)	-2.452±0.037	-114.505±0.093	-5.562±0.055	-44.171±0.068	1
π^\dagger	Gaia Parallax (mas)	2.1554±0.0485	12.4148±0.0786	3.23058±0.0779	4.74218±0.05398	1

NOTES: The uncertainties of the photometry have a systematic error floor applied.

‡ RA and Dec are in epoch J2000. The coordinates come from Vizier where the Gaia RA and Dec have been precessed to J2000 from epoch J2015.5.

† Parallaxes here are corrected for the 82 μ s offset reported in [Stassun & Torres \(2018\)](#).

References: ¹Gaia Collaboration et al. (2018), ²Høg et al. (2000), ³Cutri et al. (2003), ⁴Zacharias et al. (2017)

vey Satellite (*TESS*, [Ricker et al. 2015](#)), as well as ground-based transit surveys like WASP ([Butters et al. 2010](#)), HATNET ([Bakos et al. 2010](#)), KELT ([Pepper et al. 2007, 2012](#)), MEarth ([Irwin et al. 2015; Dittmann et al. 2017](#)), and TRAPPIST ([Gillon et al. 2011](#)), and more recently, SPECULOOS ([Delrez et al. 2018](#)) and NGTS ([Wheatley et al. 2018](#)). These future facilities will require efficient scheduling, meaning the transit times predicted for exoplanet targets will need to be both accurate and precise. The high cost of operations for *JWST* particularly will necessitate precise ephemerides in order to use resources efficiently. Currently, the predicted transit times of many previously discovered planets (when projected through the *JWST* era) have ephemerides too imprecise to meet these demands.

The *Kepler* space telescope, NASA's first mission aimed at discovering transiting exoplanets, led to the discovery of over 2300 planets and the identification of thousands more

candidates ([Thompson et al. 2018](#)).¹ However, by the end of the primary mission in early 2013, a second reaction wheel on the spacecraft failed, compromising the spacecraft's ability to point. The *K2* mission ([Howell et al. 2014](#)) solved the spacecraft's pointing ability by balancing solar radiation pressure to stabilize the *Kepler* spacecraft. This led to a survey of the ecliptic plane, providing another opportunity to discover planets around bright, nearby stars. Before being retired in 2018, *K2* completed 18 full observing campaigns of approximately 80 days, discovering over 400 additional planets.¹ Many of the planets discovered by *K2* now have stale ephemerides, since some were observed as early as 2014 and the first was announced in December of 2014 ([Vanderburg et al. 2015](#)). This hinders our ability to precisely predict upcoming times of transit. Previous efforts addressing this issue have used follow up transit observations, such as from NASA's Spitzer Space Telescope, to re-

¹ exoplanetarchive.ipac.caltech.edu

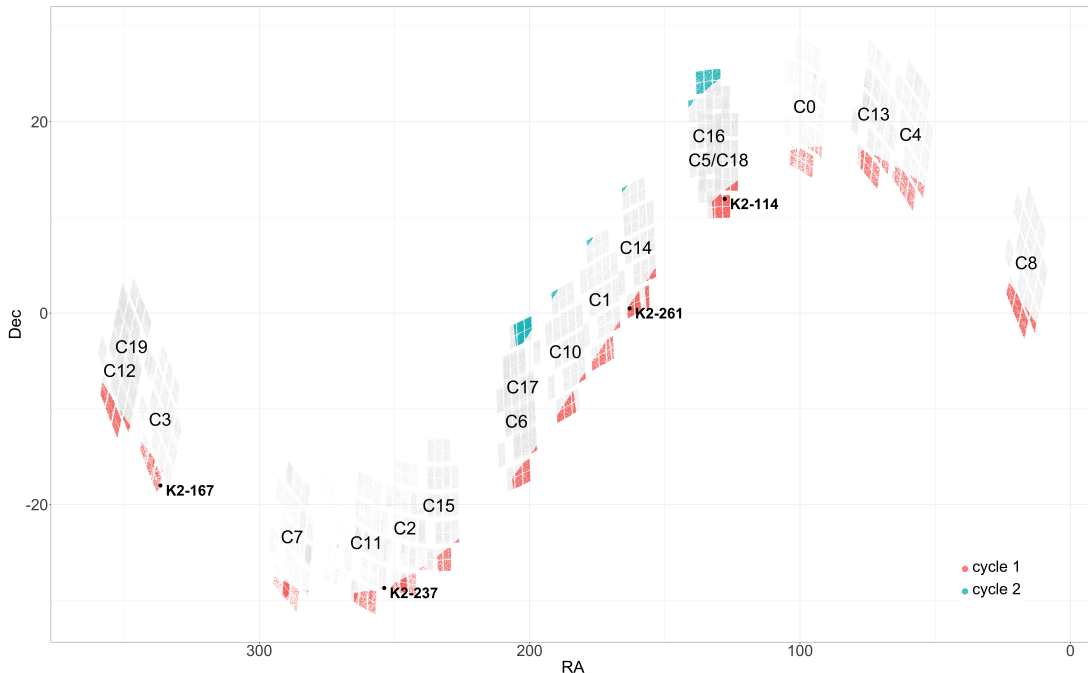


Figure 1. Map of K2 targets that were observed in *TESS* years 1 (red) and 2 (blue).

fine K2 ephemerides (e.g. [Benneke et al. 2017](#); [Livingston et al. 2019](#)).

The Transiting Exoplanet Survey Satellite (*TESS*) provides an opportunity to update the ephemerides for many more K2 planets and also to improve the stellar and planetary parameters. *TESS* launched in April 2018 with the goal of discovering thousands of new planets around nearby, bright stars ([Ricker et al. 2015](#)). Now in the second year of its primary mission, *TESS* has so far discovered 51 planets appearing in the refereed literature^{1 2} (e.g. [Huang et al. 2018](#); [Vanderspek et al. 2019](#); [Rodriguez et al. 2019](#)) and over a thousand planet candidates³ (N. Guerrero et al. *submitted*). Although *TESS*'s on-sky footprint avoids the ecliptic plane in its primary mission, the K2 fields extend far enough out of the ecliptic to partially overlap with the *TESS* fields, and for K2 campaign 19 it was simultaneous ([Barclay & Barentsen 2018](#)). [Dotson et al. \(2020\)](#) compared the K2 target list with the planned *TESS* observations using the *TESS* Visibility Tool⁴ and concluded that during Cycle 1 (the first year) of the primary mission, *TESS* observed 39,451 K2 targets. By the end of Cycle 2, *TESS* will have observed a total of 48,633 K2 targets (see Figure 1), and in the first approved extended mission, it will observe over half of the K2 footprint ([Dotson et al. 2020](#)).⁵ Additionally, the *TESS* ephemerides, specifically systems with

only a ~ 27 day baseline, will degrade in a similar manner as K2 systems, and will also require future follow up observations to update the predicted times of transit ([Dragomir et al. 2019](#)).

In this paper we present a case study of the potential improvement in precision of future transits for K2 planets observed by *TESS*. Using observations from both missions, we can significantly improve the precision and accuracy of the ephemeris for known planetary systems discovered by K2. Additionally, the combined K2 and *TESS* data provide the opportunity to potentially discover new planets in these systems and has already aided in the vetting of *TESS* planet candidates. We jointly fit the *TESS* and K2 data, with archival radial velocities, to provide updated ephemerides and system parameters for four planetary systems discovered by K2: K2-114, K2-167, K2-237, and K2-261 ([Livingston et al. 2018](#); [Mayo et al. 2018](#); [Smith et al. 2019](#); [Soto et al. 2018](#); [Johnson et al. 2018](#)). These four systems were some of the first K2 targets to be observed by *TESS* and were chosen because they were clearly detected in *TESS*. Using our analysis, we significantly improve the precision of predicted transit times as projected through the *JWST* era, in some cases by an order of magnitude.

2. OBSERVATIONS AND ARCHIVAL DATA

In this section, we discuss the observations used in our analysis to refine and improve the ephemerides and system parameters for future follow-up efforts. See Table 1 for the literature kinematics and magnitudes for K2-114, K2-167, K2-237, and K2-261.

² as of June 4, 2020

³ exofop.ipac.caltech.edu/tess

⁴ heasarc.gsfc.nasa.gov/cgi-bin/tess/webtess/wtv.py

⁵ heasarc.gsfc.nasa.gov/docs/tess/announcement-of-the-tess-extended-mission.html

Table 2. The dates of the *TESS* and *K2* observations.

Target	K2 Campaign	K2 Dates (UT)	TESS Sector	TESS Dates (UT)
K2-114	5	2015 April 27 to July 10	7	2019 January 07 to February 02
	18	2018 May 13 to July 2		
K2-167	3	2014 November 17 to 2015 January 23	2	2018 August 22 to September 20
K2-237	11	2016 September 26 to December 07	12	2019 May 21 to UT 2019 June 19
K2-261	14	2017 June 02 to August 19	9	2019 February 28 to March 26

2.1. *K2* Photometry

During its lifetime, *K2* achieved similar precision (after applying corrections) to that of the original four year *Kepler* prime mission (Vanderburg et al. 2016b). For each target, we extracted the light curve from the target pixel files, calibrated by the *Kepler* pipeline (Jenkins et al. 2010) and accessed through the Mikulski Archive for Space Telescopes (MAST).⁶ We followed the technique described in Vanderburg & Johnson (2014) and Vanderburg et al. (2016a) to reprocess the light curve, fitting the known planet transit while simultaneously removing known *K2* systematics from spacecraft motion and fitting variability induced by the host star. We used the default photometric apertures chosen by the pipeline for all planets except for K2-237, where we chose smaller apertures to reduce contamination from nearby stars (see Section 2.3). We applied a correction to the K2-237 light curve to account for the remaining contaminating light we could not avoid using the measured *Kepler* pixel response function (Bryson et al. 2010) and the *Kepler* band magnitudes of nearby stars to calculate the expected flux contamination. The other three stars are sufficiently isolated that the dilution corrections are negligible. We then flattened the light curve, removing the stellar variability with a spline with break points every 0.75 days. The *K2* phase-folded transit light curves are shown in gold in Figure 2. For the global fitting in Section 3, we used a baseline of one transit duration on either side of the full transit, removing the remaining out-of-transit data. Each *K2* target was observed in 30-minute cadence, with the exception of the C18 observations of K2-114, which were taken at 1-minute cadence. See Table 2 for the times and campaigns for each target.

2.2. *TESS* Photometry

All four of the *K2* systems (K2-114, K2-167, K2-237, & K2-261) were pre-selected for two-minute cadence observations by *TESS* (K2-114 b was a Guest Investigator (GI) target, G011183 PI Kane). Each system was observed by Camera 1 during one of *TESS*' ~ 27 -day sectors (see Table 2 for the dates of the *TESS* observations). For each target, we accessed the *TESS* light curves as generated by NASA's Sci-

ence Processing Operations Center (SPOC) pipeline through the Lightkurve software package (Lightkurve Collaboration et al. 2018). After receiving raw data from the spacecraft, SPOC processes the images, extracts photometry, and removes systematic errors (Jenkins et al. 2016). Specifically, the pipeline performs pixel-level calibrations, identifies an optimal photometric aperture and extracts the light curve, and estimates and corrects for flux contamination from nearby stars. Using the Presearch Data Conditioning (PDC) module, instrumental artifacts are removed (Smith et al. 2012; Stumpe et al. 2012, 2014). The final light curves are searched for transit crossing events (TCEs) using the SPOC Transiting Planet Search (TPS, Jenkins 2002). The *K2* targets we analyzed in this work were assigned a *TESS* Object of Interest (TOI) number as part of the TOI catalog (N. Guerrero et al. *submitted*): K2-114 b = TOI 514.01, K2-167 b = TOI 1407.01, K2-237 b = TOI 1049.01, and K2-261 b = TOI 685.01. After downloading the SPOC light curve files, we removed astrophysical variability using the Lightkurve *flatten* function, which removes low frequency trends using SciPy's Savitzky-Golay filter (Savitzky & Golay 1964; Lightkurve Collaboration et al. 2018; Virtanen et al. 2020). In our experience removing lower frequency trends, we find no significant difference between this and a spline filter. The *TESS* lightcurve of K2-237 also revealed a short-period stellar variability with a period of 0.53 days, which we attributed to the nearby RR Lyrae stars (see Section 2.3). We removed this short-period stellar variability by dividing out the phase-folded *TESS* light curve at the measured variability period. The final *TESS* phase-folded transits are shown in blue in Figure 2. We use these results for fitting each system in Section 3.

2.3. Stellar Variability in K2-237

To search for periodic photometric variability, we analyzed the unflattened PDC version of each *K2* and *TESS* light curve. First, we divided out the best-fit low-order polynomials, which effectively removed the flux trends, and retained any higher-frequency variability. The *K2* light curve of K2-237 revealed a distinct M-shaped periodic modulation signal with an amplitude of around 3500 ppm. Both, the Lomb-Scargle and autocorrelation analysis indicated a period of 5.1 ± 0.5 days during the first part of the Campaign 11 light

⁶ mast.stsci.edu/portal/Mashup/Clients/Mast/Portal.html

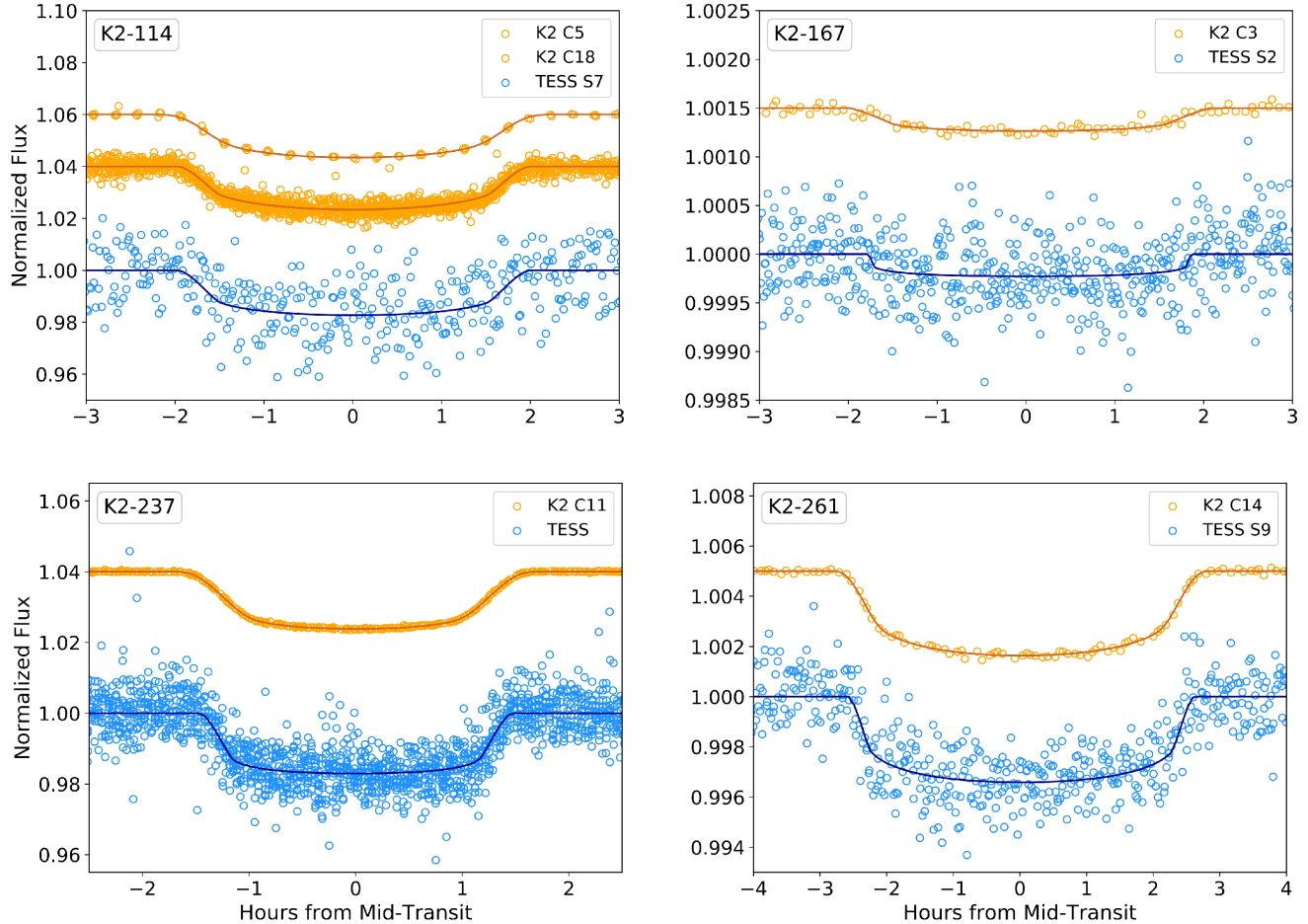


Figure 2. The phase folded (blue) *TESS* and (gold) *K2* transits for (top-left) K2-114 b, (top-right) K2-167 b, (bottom-left) K2-237 b, and (bottom-right) K2-261 b. The legend indicates that the *K2* campaign and *TESS* sector the target was observed in. The solid color line on each transit represents the best-fit transit model from our EXOFASTv2 global fit (see Section 3). A vertical offset has been applied to the *K2* data in each system for visual clarity. K2-114 b was observed at 30-minute cadence in *K2* campaign 5 and then reobserved at 1-minute cadence in campaign 18.

curve. The modulation in the second part is less coherent. This is likely rotational modulation, and it being less coherent in the second part is likely due to starspot evolution, and therefore the measured rotational period of 4.7 days is less accurate but still consistent with the measurement from the first part. This is consistent with previous analyses of the *K2* observations of K2-237, which also found a 5.1-day signal of stellar rotation (Soto et al. 2018; Smith et al. 2019). We removed the modulation prior to including the data set in the global fit (see Section 2.1).

The 5-day rotational modulation signal was not detectable in the *TESS* lightcurve of K2-237. This may be due to the fact that the *TESS* and *K2* baselines do not temporally overlap and are separated by nearly 900 days. Starspot evolution can lead to changes in observed period and amplitude, and spot contrasts in the redder *TESS* bandpass can also sup-

press amplitudes (Oelkers et al. 2018). Instead, the *TESS* light curve, shown in full in Figure 3, revealed an RR-Lyrae-like signal with a period of 0.527 ± 0.004 days and an amplitude of 4200 ppm. This signal was not seen in the *K2* light curve. Given that the *TESS* pixel scale of 21 arcsec is significantly larger than the *K2* pixel scale of 4 arcsec, we attributed the 0.53-day variability signal to one of the nearby contaminating stars, which was confirmed by the SPOC Data Validation (Twicken et al. 2018; Li et al. 2019). Specifically, in addition to detecting the signature of TOI 1049.01 (K2-237 b), a second TCE was generated with a period of 0.529 days in the SPOC Data Validation component. The difference image for this TCE in the SPOC data validation report showed a single pixel at the upper edge of the postage stamp that was highly anti-correlated with the transit signature. There was only one TIC object on that pixel (TIC 16288004). This in-

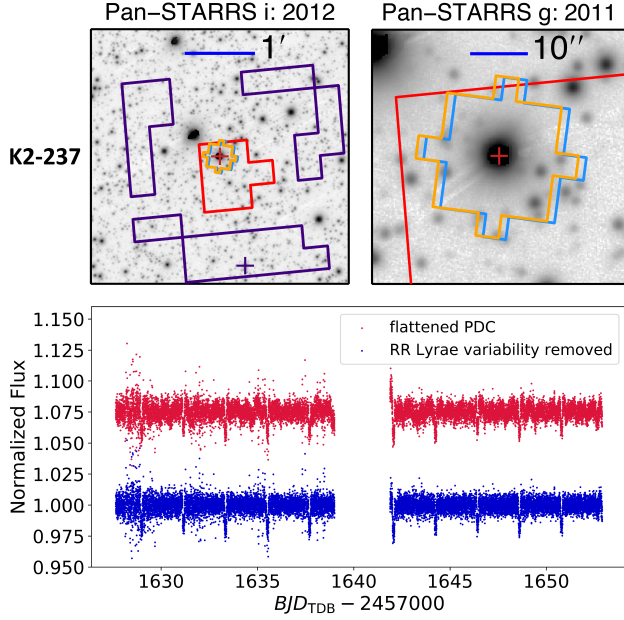


Figure 3. Pan-STARRS images of the field around K2-237 are shown in the upper panel (Flewelling et al. 2016), including the SPOC aperture (red outline), the SPOC background apertures (purple outline), the position of the blended RR Lyrae (purple cross), and the two parts of K2 Campaign 11 apertures (blue and orange outlines). The lower panel shows the RR Lyrae signal in the TESS light curve: the flattened SPOC PDC light curve is shown before (red) and after (blue) removal of the 0.53-day variability signal.

indicates that the 0.527-day signature was introduced into the light curve through the background correction. Simbad indicates that the star at the coordinates of TIC 16288004 is a known RR Lyr variable, KY Oph ($96''$ from K2-237, see Figure 3). We did not detect any periodic variability in any of the light curves of the other three stars.

2.4. Archival Spectroscopy

For three of the four K2 systems analyzed in this work (all but K2-167), we obtained the archival radial velocity (RV) measurements from the literature (Figure 4). We combined these archival observations with the transit light curves extracted from the photometric observations from K2 and TESS to provide updated system parameters and ephemerides for future follow up efforts. For K2-261 b we used 12 RV observations from the Fibre-fed Échelle Spectrograph (FIES; Frandsen & Lindberg 1999), 9 RVs from the High Accuracy Radial velocity Planet Searcher for the Northern hemisphere (HARPS-N; Cosentino et al. 2012), and 11 RVs from the High Accuracy Radial velocity Planet Searcher (HARPS; Mayor et al. 2003) that were used in the discovery paper (Johnson et al. 2018). For K2-114, we used the 5 RV observations from the High Resolution Echelle Spectrometer (HIRES, Vogt et al. 1994) on the Keck I telescope (Shporer

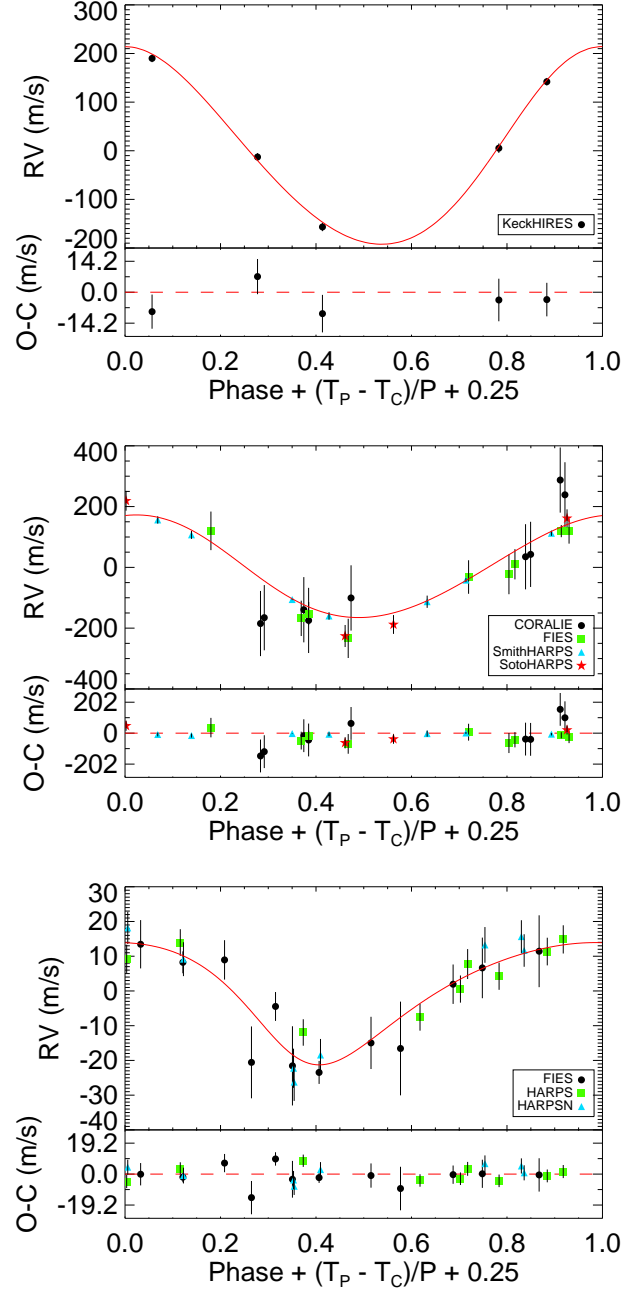


Figure 4. The archival radial velocity measurements for K2-114 b (top), K2-237 b (middle), and K2-261 b (bottom), phase-folded to the best fit period from our EXOFASTv2 global fit. See Section 2.4 for a description of the literature RVs. The EXOFASTv2 model is shown in red and the residuals to the best-fit are shown below each plot. T_p is time of periastron and T_c is time of conjunction (transit).

et al. 2017). With only 5 observations, the global fit has fewer degrees of freedom, and therefore a limited ability to constrain the jitter within the fit. Therefore, we provide a conservative uniform bound on the jitter variance of the fit of $300 (m/s)^2$ on the KECK HIRES RVs for K2-114 b. The

discovery of K2-237 b was led by two separate teams (Soto et al. 2018; Smith et al. 2019), with RV observations coming from three separate facilities: FIES (10), HARPS (11), and the CORALIE (9) spectrograph (Queloz et al. 2000). The 11 RV observations from HARPS were treated separately, with 4 observations coming from the Soto et al. (2018) reduction and 7 coming from the reduction done by Smith et al. (2019). These observations were reduced in different manners, so we treated them as separate facilities in our global model (with unique jitter and gamma parameters).

K2-167 b was statistically validated as part of a larger effort for K2 campaigns 0 to 10 (Mayo et al. 2018). There was no mass measured for this system; we did not have any RVs to include in our fit. We also used the determined metallicity from the discovery papers as a prior on our global fit (see Section 3). Specifically, we use an [Fe/H] metallicity of 0.410 ± 0.037 dex (K2-114, Shporer et al. 2017), 0.45 ± 0.08 dex (K2-167, Mayo et al. 2018), 0.14 ± 0.05 dex (K2-237, Soto et al. 2018), and 0.36 ± 0.06 dex (K2-261, Johnson et al. 2018).

3. EXOFASTv2 GLOBAL FITS

The advent of new software packages allows us to more easily combine the archival observations (K2 photometry and RVs) with new data from TESS. Additionally, with the ongoing success of the Gaia mission, we now know the distances to almost every known planet host, allowing us to accurately characterize the host star through a combination of spectral energy distributions, Gaia parallaxes, and updated stellar models. To refine the ephemerides and system parameters of the four K2 systems, we used the exoplanet fitting suite, EXOFASTv2 (Eastman et al. 2013; Eastman 2017; Eastman et al. 2019). In each case other than K2-237 (see Section 3.1), we first conducted a preliminary fit of the entire system using EXOFASTv2 to get an estimate for the surface gravity of the host star. We then performed a fit of the spectral energy distribution (SED) of the host star with EXOFASTv2, using the determined stellar surface gravity ($\log g$) as a starting point with a loose 0.25 dex Gaussian prior. We also included Gaussian priors on the stellar metallicity ([Fe/H]) from the discovery paper (see Section 2.4) and parallax from Gaia, and constrained the maximum line of sight extinction (A_V) for each system using the galactic dust maps from Schlegel et al. (1998) and Schlafly & Finkbeiner (2011). The precision on fundamental stellar parameters like [Fe/H] and the stellar effective temperature (T_{eff}) should be limited to the precision of stellar radii measurements from interferometry (White et al. 2018). The SED fit provided values on the stellar effective temperature (T_{eff}) and stellar radius (R_*) that were too precise, so we used the resulting T_{eff} and R_* with the adopted fractional errors of 1.5% (for T_{eff}) and 3.5% (for R_*) as Gaussian priors on the full global fit. This resulted in a prior on

R_* and T_{eff} of $0.810 \pm 0.0284 R_\odot$ and 4930.0 ± 82.0 K for K2-114, $1.664 \pm 0.058 R_\odot$ and 6182.0 ± 93.0 K for K2-167, and $1.467 \pm 0.052 R_\odot$ and 5449.0 ± 82.0 K for K2-261. Specifically, for each system we simultaneously fit the TESS (see Section 2.2) and K2 (see Section 2.1) photometry with the archival RV data (see Section 2.4). In the case of K2-167, no radial velocity observations are available (Mayo et al. 2018), so we globally modeled only the photometric data. Within the fit, the mass, radius, and age of the host star are constrained by the MESA Isochrones and Stellar Tracks (MIST) stellar evolution models (Dotter 2016; Choi et al. 2016; Paxton et al. 2011, 2013, 2015). In every case, we allow EXOFASTv2 to fit a dilution term to the TESS light curve, using the K2 lightcurve as a reference. In all cases, the dilution term on the TESS light curve is consistent with zero at $< 2\sigma$. Since we adjusted the K2 light curve from the standard pipeline (see Section 2.1), we allow EXOFASTv2 to fit a dilution term for the K2 lightcurve as well in this fit but bound it with a conservative 5% prior around zero. The dilution term for the K2 lightcurve is consistent with zero at $< 1\sigma$. In all cases, we aimed for strict convergence criteria that required a Gelman–Rubin statistic (Gelman & Rubin 1992) of less than 1.01 and at least 1000 independent draws in each parameter. The results are shown in Figures 2 and 4, and Tables 3 and 4.

3.1. K2-237 Global Fit

For the K2-237 system, we ran the full global model slightly differently than as described in the previous section. Specifically, the SED was far less constraining on the fundamental stellar parameters, due to the target lacking Tycho B_T and V_T magnitudes and the maximum line-of-sight extinction being higher than is typical. Therefore, we included the SED within the global model, placing Gaussian priors on the Gaia parallax and the [Fe/H] from Soto et al. (2018) (see Section 2.4) and an upper limit on the maximum line of sight extinction (A_V) from Schlegel et al. (1998) and Schlafly & Finkbeiner (2011). The resulting parameters have larger uncertainties than for the other systems.

3.2. K2-261 Bimodality

When analyzing the probability distribution function (PDF) for the host star’s mass and age for K2-261, we noticed a bimodality (see Figure 5). The peaks are centered at $1.09 M_\odot$ (9.3 Gyr) and $1.27 M_\odot$ (4.84 Gyr), with the lower mass solution having a 76.1% probability of being correct from our analysis. With no optimal way to properly represent the PDF due to the bimodality, we split the host star’s mass at the minimum value between the two peaks in the posterior distribution at $M_* = 1.19 M_\odot$, and extracted two solutions, one for each mass peak. The two solutions are shown in Table 3. There are no significant differences in the systematic parameters resulting from the two solutions; we believe the

Table 3. Median values and 68% confidence interval for global models

Parameter	Description (Units)	K2-114	K2-167	K2-237	K2-261*	
Probability ..		100 %	100 %	100 %	76.1 %	23.9 %
Stellar Parameters:						
M_*	Mass (M_\odot)	$0.860^{+0.039}_{-0.034}$	$1.347^{+0.067}_{-0.070}$	$1.263^{+0.052}_{-0.068}$	$1.091^{+0.049}_{-0.051}$	$1.266^{+0.043}_{-0.041}$
R_*	Radius (R_\odot)	$0.824^{+0.024}_{-0.023}$	$1.459^{+0.052}_{-0.051}$	$1.261^{+0.031}_{-0.029}$	$1.642^{+0.058}_{-0.059}$	$1.639^{+0.058}_{-0.055}$
L_*	Luminosity (L_\odot)	$0.358^{+0.033}_{-0.029}$	$2.78^{+0.27}_{-0.25}$	$2.35^{+0.30}_{-0.27}$	$2.14^{+0.20}_{-0.19}$	$2.22^{+0.21}_{-0.19}$
ρ_*	Density (cgs)	$2.17^{+0.18}_{-0.17}$	$0.612^{+0.069}_{-0.062}$	$0.888^{+0.065}_{-0.075}$	$0.347^{+0.038}_{-0.032}$	$0.406^{+0.038}_{-0.035}$
$\log g_*$	Surface gravity (cgs)	4.542 ± 0.025	$4.240^{+0.033}_{-0.034}$	$4.339^{+0.022}_{-0.031}$	$4.045^{+0.031}_{-0.030}$	4.112 ± 0.025
T_{eff}	Effective Temperature (K)	4920^{+70}_{-69}	6170^{+92}_{-93}	6360^{+190}_{-200}	5447 ± 77	5502 ± 73
[Fe/H]	Metallicity (dex)	$0.408^{+0.037}_{-0.036}$	$0.425^{+0.058}_{-0.069}$	$0.137^{+0.050}_{-0.049}$	$0.360^{+0.058}_{-0.059}$	$0.385^{+0.056}_{-0.058}$
[Fe/H] ₀	Initial Metallicity	$0.378^{+0.046}_{-0.047}$	$0.432^{+0.045}_{-0.059}$	$0.157^{+0.050}_{-0.055}$	$0.359^{+0.057}_{-0.058}$	$0.382^{+0.053}_{-0.054}$
Age	Age (Gyr)	$7.2^{+4.4}_{-4.5}$	$1.9^{+1.1}_{-1.3}$	$1.02^{+1.6}_{-1.74}$	$9.3^{+2.0}_{-1.5}$	$4.84^{+0.68}_{-0.71}$
EEP	Equal Evolutionary Phase	346^{+22}_{-28}	344^{+28}_{-23}	324^{+20}_{-40}	$455.6^{+8.0}_{-8.0}$	$415.5^{+8.1}_{-12}$
A_V	V-band extinction (mag)	—	—	$0.31^{+0.12}_{-0.13}$	—	—
σ_{SED}	SED photometry error scaling	—	—	$1.72^{+0.72}_{-0.43}$	—	—
Planetary Parameters:						
b						
P	Period (days)	11.3909311 ± 0.0000034	9.978572 ± 0.000022	$2.18053539^{+0.00000086}_{-0.00000085}$	11.633480 ± 0.000017	11.633480 ± 0.000017
R_p	Radius (R_J)	0.931 ± 0.031	$0.202^{+0.013}_{-0.010}$	$1.445^{+0.049}_{-0.045}$	0.849 ± 0.034	$0.846^{+0.035}_{-0.032}$
M_p	Mass (M_J)	2.01 ± 0.12	—	$1.363^{+0.11}_{-0.092}$	$0.189^{+0.025}_{-0.026}$	$0.213^{+0.026}_{-0.028}$
T_C	Time of conjunction (BJD _{TDB})	$2457140.32399 \pm 0.00023$	2456979.9326 ± 0.0020	$2457656.463880^{+0.000037}_{-0.000036}$	$2457906.84104^{+0.00030}_{-0.00034}$	$2457906.84103^{+0.00028}_{-0.00032}$
T_0^\dagger	Optimal conjunction Time (BJD _{TDB})	$2457664.30682^{+0.00017}_{-0.00016}$	2457309.2254 ± 0.0018	$2457702.255123^{+0.000032}_{-0.000031}$	$2457976.64193^{+0.00028}_{-0.00032}$	$2457976.64191^{+0.00026}_{-0.00030}$
a	Semi-major axis (AU)	$0.0943^{+0.0014}_{-0.0013}$	$0.1002^{+0.0016}_{-0.0018}$	$0.03558^{+0.00048}_{-0.00065}$	$0.1034^{+0.0015}_{-0.0016}$	0.1087 ± 0.012
i	Inclination (Degrees)	$89.21^{+0.21}_{-0.14}$	$87.43^{+1.5}_{-0.61}$	$88.03^{+1.1}_{-0.82}$	$88.07^{+1.1}_{-0.64}$	$88.37^{+0.98}_{-0.62}$
e	Eccentricity	$0.081^{+0.031}_{-0.030}$	$0.40^{+0.31}_{-0.22}$	$0.047^{+0.034}_{-0.028}$	$0.288^{+0.063}_{-0.069}$	0.252 ± 0.063
ω_*	Argument of Periastron (Degrees)	-51^{+21}_{-12}	20^{+110}_{-170}	74 ± 38	131^{+16}_{-17}	137^{+16}_{-18}
T_{eq}	Equilibrium temperature (K)	700 ± 14	1135 ± 24	1828^{+48}_{-46}	1046^{+21}_{-22}	1030 ± 21
K	RV semi-amplitude (m/s)	200^{+10}_{-11}	—	183^{+15}_{-11}	$16.8^{+2.2}_{-2.3}$	$16.9^{+2.1}_{-2.2}$
$\log K$	Log of RV semi-amplitude	$2.303^{+0.022}_{-0.023}$	—	$2.263^{+0.035}_{-0.028}$	$1.224^{+0.054}_{-0.063}$	$1.227^{+0.051}_{-0.061}$
R_p/R_*	Radius of planet in stellar radii	$0.1162^{+0.0014}_{-0.0016}$	$0.01416^{+0.00082}_{-0.00046}$	$0.1177^{+0.0027}_{-0.0026}$	$0.05304^{+0.0011}_{-0.00073}$	$0.05292^{+0.0010}_{-0.00065}$
a/R_*	Semi-major axis in stellar radii	$24.63^{+0.68}_{-0.65}$	$14.77^{+0.53}_{-0.52}$	$6.07^{+0.14}_{-0.18}$	$13.54^{+0.48}_{-0.44}$	$14.27^{+0.43}_{-0.42}$
δ	Transit depth (fraction)	$0.01351^{+0.00033}_{-0.00036}$	$0.000201^{+0.000024}_{-0.000013}$	$0.01385^{+0.00065}_{-0.00060}$	$0.002813^{+0.00011}_{-0.000077}$	$0.002801^{+0.00011}_{-0.000068}$
τ	Ingress/egress transit duration (days)	0.0195 ± 0.0015	$0.00269^{+0.00020}_{-0.00060}$	$0.01348^{+0.00056}_{-0.00047}$	$0.0122^{+0.0023}_{-0.0014}$	$0.0119^{+0.0022}_{-0.0012}$
T_{14}	Total transit duration (days)	0.1654 ± 0.0012	0.1511 ± 0.0038	$0.12199^{+0.00039}_{-0.00037}$	$0.2141^{+0.0019}_{-0.0014}$	$0.2140^{+0.0018}_{-0.0013}$
T_{FWHM}	FWHM transit duration (days)	$0.14583^{+0.00088}_{-0.00084}$	0.1477 ± 0.0035	$0.10849^{+0.00026}_{-0.00028}$	0.20175 ± 0.00084	0.20181 ± 0.00083
b	Transit Impact parameter	$0.359^{+0.068}_{-0.10}$	$0.47^{+0.26}_{-0.32}$	$0.20^{+0.085}_{-0.12}$	$0.35^{+0.15}_{-0.21}$	$0.32^{+0.16}_{-0.20}$
b_S	Eclipse impact parameter	$0.316^{+0.048}_{-0.078}$	$0.51^{+0.23}_{-0.33}$	$0.216^{+0.084}_{-0.12}$	$0.53^{+0.14}_{-0.30}$	$0.46^{+0.14}_{-0.27}$
τ_S	Ingress/egress eclipse duration (days)	$0.01691^{+0.0011}_{-0.00098}$	$0.0039^{+0.0013}_{-0.0019}$	$0.01450^{+0.0010}_{-0.00077}$	$0.0206^{+0.0032}_{-0.0024}$	$0.0179^{+0.0021}_{-0.0016}$
$T_{S,14}$	Total eclipse duration (days)	$0.1481^{+0.0090}_{-0.0079}$	$0.156^{+0.083}_{-0.033}$	$0.1303^{+0.0087}_{-0.0069}$	$0.298^{+0.058}_{-0.045}$	$0.285^{+0.041}_{-0.038}$
$T_{S,FWHM}$	FWHM eclipse duration (days)	$0.1311^{+0.0084}_{-0.0071}$	$0.152^{+0.084}_{-0.032}$	$0.1158^{+0.0079}_{-0.0063}$	$0.278^{+0.059}_{-0.047}$	$0.267^{+0.042}_{-0.039}$
$\delta_{S,3.6\mu m}$	Blackbody eclipse depth at $3.6\mu m$ (ppm)	$53.4^{+6.0}_{-5.6}$	$5.44^{+0.73}_{-0.53}$	1507^{+85}_{-79}	$66.3^{+5.4}_{-5.2}$	$61.1^{+5.1}_{-4.6}$
$\delta_{S,4.5\mu m}$	Blackbody eclipse depth at $4.5\mu m$ (ppm)	129 ± 11	$8.70^{+1.1}_{-0.76}$	1900^{+100}_{-93}	$111.2^{+7.7}_{-7.3}$	$103.8^{+7.3}_{-6.5}$
ρ_p	Density (cgs)	$3.08^{+0.37}_{-0.33}$	—	$0.562^{+0.066}_{-0.061}$	$0.381^{+0.071}_{-0.062}$	$0.434^{+0.074}_{-0.070}$
$\log g_p$	Surface gravity	3.759 ± 0.038	—	$3.210^{+0.040}_{-0.039}$	$2.812^{+0.063}_{-0.067}$	$2.866^{+0.059}_{-0.067}$
$\langle F \rangle$	Incident Flux ($10^9 \text{ erg s}^{-1} \text{ cm}^{-2}$)	$0.0543^{+0.0046}_{-0.0042}$	$0.317^{+0.049}_{-0.078}$	$2.53^{+0.28}_{-0.25}$	$0.250^{+0.021}_{-0.020}$	$0.239^{+0.020}_{-0.019}$
T_p	Time of Periastron (BJD _{TDB})	$2457136.05^{+0.65}_{-0.43}$	$2456970.01^{+0.85}_{-0.86}$	2457656.38 ± 0.21	$2457895.93^{+0.33}_{-0.29}$	$2457896.10^{+0.39}_{-0.32}$
T_S	Time of eclipse (BJD _{TDB})	$2457146.38^{+0.10}_{-0.12}$	2456984.9 ± 3.0	$2457657.565^{+0.034}_{-0.025}$	$2457899.68^{+0.56}_{-0.65}$	$2457899.73^{+0.50}_{-0.59}$
T_A	Time of Ascending Node (BJD _{TDB})	2457137.45 ± 0.11	$2456978.1^{+1.2}_{-1.5}$	$2457658.129^{+0.031}_{-0.027}$	$2457904.23^{+0.36}_{-0.39}$	$2457904.06^{+0.34}_{-0.37}$
T_D	Time of Descending Node (BJD _{TDB})	$2457143.59^{+0.16}_{-0.18}$	$2456981.8^{+1.5}_{-1.2}$	$2457656.993^{+0.019}_{-0.026}$	$2457896.86^{+0.28}_{-0.25}$	$2457896.99^{+0.27}_{-0.25}$
$e \cos \omega_*$	$0.050^{+0.014}_{-0.017}$	-0.00 ± 0.49	$0.008^{+0.025}_{-0.018}$	$-0.179^{+0.075}_{-0.088}$	$-0.173^{+0.067}_{-0.081}$
$e \sin \omega_*$	$-0.062^{+0.036}_{-0.034}$	$0.08^{+0.20}_{-0.28}$	$0.034^{+0.033}_{-0.029}$	$0.209^{+0.059}_{-0.069}$	$0.170^{+0.052}_{-0.067}$
$M_p \sin i$	Minimum mass (M_J)	2.01 ± 0.12	—	$1.362^{+0.11}_{-0.092}$	$0.189^{+0.025}_{-0.026}$	$0.212^{+0.026}_{-0.027}$
M_p/M_*	Mass ratio	0.00222 ± 0.00012	—	$0.001034^{+0.000090}_{-0.000066}$	$0.000166^{+0.000021}_{-0.000022}$	$0.000160^{+0.000020}_{-0.000021}$

NOTES:

*The global solution for K2-261 b showed a clear bimodality in the host star's mass and age (see Figure 5 and §3.2). We extract a solution and a probability for each peak, which are both shown in the table. The lower stellar mass (and high age) solution is significantly more likely, but both solutions are presented for future studies on K2-261 b.

See Table 3 in Eastman et al. (2019) for a list of the derived and fitted parameters in EXOFASTv2.

†Minimum covariance with period.

All values in this table for the secondary occultation are predicted values from our global analysis.

See §3 for a description of how the EXOFASTv2 fit was conducted and what priors were used for each fit.

Table 4. Median values and 68% confidence interval for global model

Wavelength Parameters:	Kepler	TESS			
K2-114					
u_1 . . . linear limb-darkening coeff . . .	0.612 ± 0.026	$0.466^{+0.051}_{-0.050}$			
u_2 . . . quadratic limb-darkening coeff	0.116 ± 0.036	$0.192^{+0.049}_{-0.050}$			
A_D . . . Dilution from neighboring stars	–	$-0.089^{+0.059}_{-0.060}$			
K2-167					
u_1 . . . linear limb-darkening coeff . . .	0.375 ± 0.051	0.257 ± 0.051			
u_2 . . . quadratic limb-darkening coeff	0.309 ± 0.050	0.304 ± 0.050			
A_D . . . Dilution from neighboring stars	–	-0.15 ± 0.12			
K2-237					
u_1 . . . linear limb-darkening coeff . . .	$0.329^{+0.014}_{-0.015}$	0.226 ± 0.042			
u_2 . . . quadratic limb-darkening coeff	$0.266^{+0.033}_{-0.034}$	0.310 ± 0.048			
A_D . . . Dilution from neighboring stars	-0.017 ± 0.047	$-0.097^{+0.053}_{-0.054}$			
K2-261					
u_1 . . . linear limb-darkening coeff . . .	$0.480^{+0.030}_{-0.031}$	0.376 ± 0.045			
u_2 . . . quadratic limb-darkening coeff	0.193 ± 0.046	0.251 ± 0.048			
A_D . . . Dilution from neighboring stars	–	-0.035 ± 0.026			
K2-114					
Velocity Parameters:		Keck HIRES			
γ_{rel} . . . Relative RV Offset (m/s)		$-41.0^{+6.8}_{-6.9}$			
σ_J . . . RV Jitter (m/s)		$11.9^{+3.8}_{-4.9}$			
σ_J^2 . . . RV Jitter Variance			140^{+100}_{-93}		
Transit Parameters:		K2 C5 (Kepler)	K2 C18 (Kepler)	TESS	
σ^2 . . . Added Variance**		$-0.000004392^{+0.000000018}_{-0.000000016}$	$0.00000082 \pm 0.00000013$	$-0.0002649^{+0.0000053}_{-0.0000050}$	
F_0 . . . Baseline flux		1.000035 ± 0.000032	0.999746 ± 0.000043	1.00010 ± 0.00039	
K2-167					
Transit Parameters:		K2 (Kepler)	TESS		
σ^2 . . . Added Variance		$-0.00000000008^{+0.0000000022}_{-0.0000000018}$	$0.0000000017^{+0.0000000051}_{-0.0000000047}$		
F_0 . . . Baseline flux		0.9999988 ± 0.0000042	1.000079 ± 0.000013		
K2-237					
Velocity Parameters:		CORALIE	FIES	HARPS (Smith)	HARPS (Soto)
γ_{rel} . . . Relative RV Offset (m/s)		-22250^{+40}_{-41}	-22501^{+16}_{-17}	$-22325.5^{+8.8}_{-9.5}$	-22252 ± 14
σ_J . . . RV Jitter (m/s)		110^{+49}_{-30}	$0.00^{+42}_{-0.00}$	18^{+23}_{-18}	$6.6^{+8.3}_{-6.6}$
σ_J^2 . . . RV Jitter Variance		12200^{+13000}_{-5800}	-30^{+1800}_{-560}	330^{+1400}_{-330}	40^{+180}_{-220}
Transit Parameters:		K2 (Kepler)	K2 (Kepler)	TESS	
σ^2 . . . Added Variance		$0.0000000056^{+0.0000000021}_{-0.0000000018}$	$0.00000000388^{+0.0000000010}_{-0.0000000094}$	$0.00001815^{+0.00000079}_{-0.00000076}$	
F_0 . . . Baseline flux		0.9999999 ± 0.0000097	0.9999946 ± 0.0000062	1.00009 ± 0.00011	
Velocity Parameters:		FIES	HARPS	HARPSN	
γ_{rel} . . . Relative RV Offset (m/s)		-13.8 ± 2.7	$3341.6^{+1.8}_{-2.1}$	$3335.0^{+2.4}_{-3.0}$	
σ_J . . . RV Jitter (m/s)		$4.2^{+4.0}_{-4.2}$	$5.0^{+2.8}_{-1.7}$	$6.8^{+4.5}_{-2.9}$	
σ_J^2 . . . RV Jitter Variance		17^{+50}_{-23}	25^{+35}_{-14}	45^{+82}_{-31}	
Transit Parameters:		K2 (Kepler)	TESS		
σ^2 . . . Added Variance		$0.00000000156^{+0.0000000064}_{-0.0000000057}$	$-0.000000174^{+0.00000044}_{-0.00000042}$		
F_0 . . . Baseline flux		0.9999978 ± 0.0000060	1.000102 ± 0.000034		

NOTES:

*The global solution for K2-261 b showed a clear bimodality in the host star’s mass and age (see Figure 5 and §3.2). The transit, velocity, and wavelength parameters shown in this table for K2-261 are for the preferred solution only.

**The RV jitter variance for K2-114 b was constrained to $300 (m/s)^2$.

See Table 3 in Eastman et al. (2019) for a list of the derived and fitted parameters in EXOFASTv2.

All values in this table for the secondary occultation are predicted values from our global analysis.

See §3 for a description of how the EXOFASTv2 fit was conducted and what priors were used for each fit.

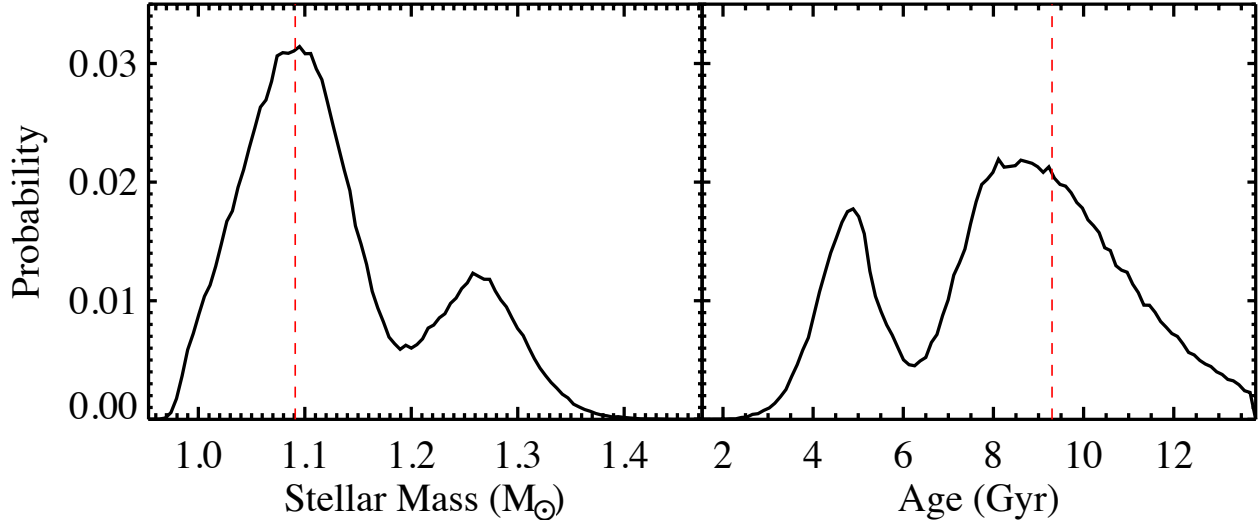


Figure 5. The probability distribution function for (Left) M_{star} and (Right) Age of K2-261 b from our global fit. The red line shows the median value for each parameter from the adopted solution (see Section 3).

bimodality is astrophysical. We adopt the solution for $M_{\star} = 1.09 M_{\odot}$, but we present both solutions, as they may be important for future studies on K2-261 b.

4. DISCUSSION

With the focus of future missions (like *JWST*) centered on studying the atmospheres of exoplanets through transmission spectroscopy, precise ephemerides and updated parameters will be crucial for scheduling and interpreting these observations. Additionally, some of these facilities will have a fixed lifetime and very high operating costs. Therefore, we want to be as efficient as possible in using these precious resources, allowing us to maximize their scientific productivity. In this paper, we have presented a case study of four known K2 planetary systems that were observed in the first year of NASA’s *TESS* mission. Our results show that combining the K2 and *TESS* data sets (along with archival spectroscopy and *Gaia* parallaxes) can reduce the uncertainty on the time of future transit by up to an order of magnitude compared to the K2 discovery results. The original and updated ephemerides, with their 1-sigma confidence intervals, are found in Table 5. As compared to the discovery ephemerides, we reduced the uncertainty on the planet’s period by roughly a factor of 66 for K2-114 (Livingston et al. 2018), a factor of 44 for K2-167 (Mayo et al. 2018), and a factor of 7 for both K2-237 (Smith et al. 2019) and K2-261 (Johnson et al. 2018). For K2-237, we compare to Smith et al. (2019) with a 4-sigma discrepancy, but our period is consistent with the other discovery ephemeris from Soto et al. (2018). The reason for the discrepancy in the discovery paper results is unclear. Our results also provide updated planetary parameters for each sys-

Table 5. The discovery ephemerides (Livingston et al. (2018), Mayo et al. (2018), Smith et al. (2019), Johnson et al. (2018)) and our updated ephemerides, and the 3-sigma uncertainty on the predicted transit times for the years 2020, 2025, and 2030.

	Discovery	Updated
K2-114		
P	$(11.391013^{+0.000224}_{-0.000225})$ d	$(11.3909311 \pm 0.0000034)$ d
T_c	$(2457151.71493 \pm 0.00069)$ BJD	$(2457140.32399 \pm 0.00023)$ BJD
$3\sigma_{2020}$	2.5 hours	3 minutes
$3\sigma_{2025}$	5.1 hours	6 minutes
$3\sigma_{2030}$	7.6 hours	8 minutes
K2-167		
P	$(9.977481^{+0.001039}_{-0.001007})$ d	$(9.978572^{+0.000022}_{-0.000024})$ d
T_c	$(2456979.93678^{+0.002518}_{-0.002443})$ BJD	$(2456979.9325 \pm 0.0023)$ BJD
$3\sigma_{2020}$	14 hours	29 minutes
$3\sigma_{2025}$	27.5 hours	47 minutes
$3\sigma_{2030}$	40.6 hours	1.1 hours
K2-237		
P^\dagger	$(2.1805577 \pm 0.0000057)$ d	$(2.18053540 \pm 0.00000085)$ d
T_c	$(2457656.4633789 \pm 0.0000048)$ BJD	$(2457656.463879^{+0.000037}_{-0.000036})$ BJD
$3\sigma_{2020}$	14 minutes	2 minutes
$3\sigma_{2025}$	34 minutes	5 minutes
$3\sigma_{2030}$	55 minutes	8 minutes
K2-261		
P	(11.63344 ± 0.00012) d	(11.633480 ± 0.000017) d
T_c	$(2457906.84084^{+0.00054}_{-0.00067})$ BJD	$(2457906.84104^{+0.00030}_{-0.00034})$ BJD
$3\sigma_{2020}$	45 minutes	7 minutes
$3\sigma_{2025}$	2.1 hours	19 minutes
$3\sigma_{2030}$	3.5 hours	30 minutes

NOTES: \dagger The new period is $\sim 4\sigma$ discrepant with Smith et al. (2019) reported period but consistent with less precise period reported by Soto et al. (2018).

tem (see Table 3), which will be important for interpreting any future follow up results.

Prior to our analysis, the uncertainties on the periods from the *K2* discovery papers propagate to produce high uncertainty (hours to days) on the predicted transit times within the next decade (see Figure 6). The 3-sigma uncertainties on the transit times predicted by the discovery ephemerides, shown in Table 5, are as high as 40.6 hours by 2030 (for K2-167). Because the addition of the *TESS* data enables such major improvement in precision on the period, the uncertainties on our predicted transit times are dominated by the uncertainty on the time of conjunction, meaning that the total uncertainty on the ephemeris grows much more slowly with time. Our results allow transit times predicted to within 30 minutes with 3-sigma confidence through at least 2030, except for K2-167 b which has a transit uncertainty of 1.1 hours in 2030 (as compared to the 40.6 hour uncertainty the discovery ephemeris would provide, see Table 5 and Figure 6). Therefore, K2-167 b would likely require additional transit follow up over the next few years to have an ephemeris precise enough to enable *JWST* observations near the expected end of the mission.

5. CONCLUSION

Using observations from the *K2* and *TESS* missions combined with archival spectroscopy, we reanalyzed four known *K2* planetary systems, providing updated system parameters and improved ephemerides for future follow up efforts. Additionally, we combined the known parallax for each system from the *Gaia* mission, allowing us to refine the stellar parameters within our global fits. We performed this case study on K2-114 b, K2-167 b, K2-237 b, and K2-261 b, and our updated ephemerides reduced the uncertainty on the orbital period by factors between 7 and 66. As a result of extending the photometric baseline for each system, we are now able to confidently predict future transit times to within ~ 1 hour through the extent of the *JWST* prime mission. Additionally, *TESS* will observe roughly half of all *K2* campaigns during the first extended mission, providing the first opportunity to perform an analysis similar to what is presented here, but on a much larger scale (hundreds of systems). This work also shows the importance of updating and maintaining accurate ephemerides, as most known exoplanets have not been re-observed, until recently by *TESS*. Therefore, it is likely that many of the known planet ephemerides are, or will be, stale, limiting the ability to conduct detailed follow-up. The *TESS* discovered exoplanet ephemerides will also quickly degrade since most will only be discovered with a ~ 27 day baseline of observations (Dragomir et al. 2019). Continued monitoring and updating of transit ephemerides will likely be necessary to conduct future targeted follow-up observations, and this paper is part of a larger effort to reanalyze previously discov-

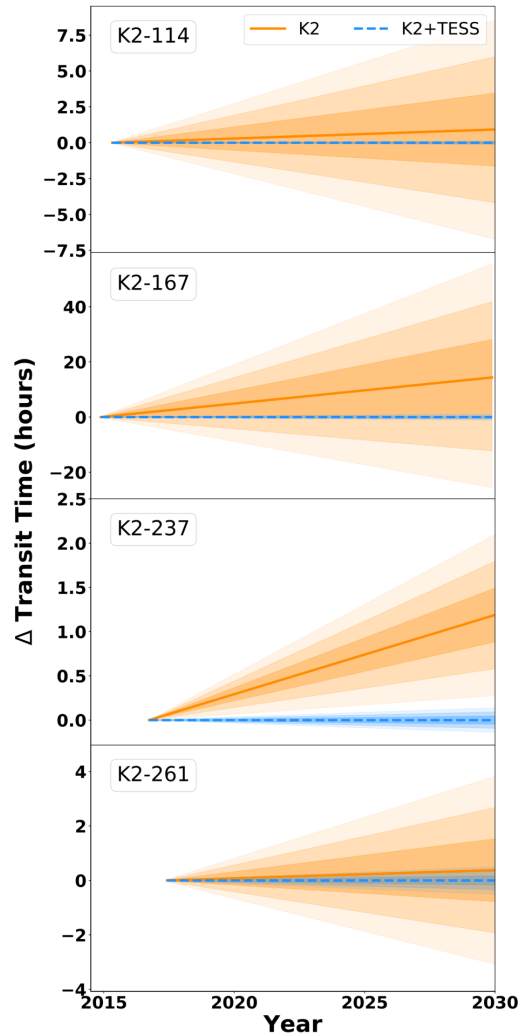


Figure 6. The difference in time of transit predicted by the *K2* discovery papers as compared to the updated predictions from this work, projected to the year 2030. The shaded regions indicate 1, 2, and 3-sigma confidence intervals. For K2-237 b, our new ephemeris is 4σ discrepant to the ephemeris from Smith et al. (2019) (shown here) but is consistent with less precise period reported by Soto et al. (2018) (not shown).

ered planets using observations from new missions like *Gaia* and *TESS*. Future work should use the method presented here to reanalyze all known exoplanets observed by *TESS*, providing the community with a larger pool of targets on which to perform detailed characterization in the era of *JWST*.

Software: Lightkurve (Lightkurve Collaboration et al. 2018), EXOFASTv2 (Eastman et al. 2013; Eastman 2017), AstroImageJ (Collins et al. 2017)

Facilities: *TESS*, *K2*, Keck (*HIRES*), La Silla 1.2m (*CORALIE*), Nordic Optical 2.56m (*FIES*), La Silla 3.6m (*HARPS*), Telescopio Nazionale Galileo 3.58m (*HARPSN*)

ACKNOWLEDGMENTS

T.D. acknowledges support from MIT's Kavli Institute as a Kavli postdoctoral fellow. This research has made use of SAO/NASA's Astrophysics Data System Bibliographic Services. This research has made use of the SIMBAD database, operated at CDS, Strasbourg, France. This work has made use of data from the European Space Agency (ESA) mission *Gaia* (<https://www.cosmos.esa.int/gaia>), processed by the *Gaia* Data Processing and Analysis Consortium (DPAC, <https://www.cosmos.esa.int/web/gaia/dpac/consortium>). Funding for the DPAC has been provided by national institutions, in particular the institutions participating in the *Gaia* Multilateral Agreement. This work makes use of observations from the LCO network. This research made use of Lightkurve, a Python package for *Kepler* and *TESS* data analysis.

Funding for the *TESS* mission is provided by NASA's Science Mission directorate. We acknowledge the use of public *TESS* Alert data from pipelines at the *TESS* Science Office and at the *TESS* Science Processing Operations Center. This research has made use of the Exoplanet Follow-up Observation Program website, which is operated by the California Institute of Technology, under contract with the National Aeronautics and Space Administration under the Exoplanet Exploration Program. Resources supporting this work were provided by the NASA High-End Computing (HEC) Program through the NASA Advanced Supercomputing (NAS) Division at Ames Research Center for the production of the SPOC data products. This paper includes data collected by the *TESS* mission, which are publicly available from the Mikulski Archive for Space Telescopes (MAST).

REFERENCES

- Bakos, G. Á., Torres, G., Pál, A., et al. 2010, *ApJ*, 710, 1724
- Barclay, T., & Barentsen, G. 2018, *Research Notes of the American Astronomical Society*, 2, 192
- Benneke, B., Werner, M., Petigura, E., et al. 2017, *ApJ*, 834, 187
- Borucki, W. J., Koch, D., Basri, G., et al. 2010, *Science*, 327, 977
- Bryson, S. T., Tenenbaum, P., Jenkins, J. M., et al. 2010, *ApJL*, 713, L97
- Butters, O. W., West, R. G., Anderson, D. R., et al. 2010, *A&A*, 520, L10
- Choi, J., Dotter, A., Conroy, C., et al. 2016, *ApJ*, 823, 102
- Collins, K. A., Kielkopf, J. F., Stassun, K. G., & Hessman, F. V. 2017, *AJ*, 153, 77
- Cosentino, R., Lovis, C., Pepe, F., et al. 2012, in *Proc. SPIE*, Vol. 8446, *Ground-based and Airborne Instrumentation for Astronomy IV*, 84461V
- Cutri, R. M., Skrutskie, M. F., van Dyk, S., et al. 2003, *VizieR Online Data Catalog*, 2246, 0
- Delrez, L., Gillon, M., Queloz, D., et al. 2018, in *Society of Photo-Optical Instrumentation Engineers (SPIE) Conference Series*, Vol. 10700, *Proc. SPIE*, 107001I
- Dittmann, J. A., Irwin, J. M., Charbonneau, D., Berta-Thompson, Z. K., & Newton, E. R. 2017, *AJ*, 154, 142
- Dotson, J., Colon, K., Barentsen, G., Gully-Santiago, M., & Hedges, C. 2020, in *American Astronomical Society Meeting Abstracts*, Vol. 52, *American Astronomical Society Meeting Abstracts*, 174.05
- Dotter, A. 2016, *ApJS*, 222, 8
- Dragomir, D., Harris, M., Pepper, J., Barclay, T., & Villanueva, Steven, J. 2019, *arXiv e-prints*, arXiv:1906.02197
- Eastman, J. 2017, *EXOFASTv2: Generalized publication-quality exoplanet modeling code*, *Astrophysics Source Code Library*, ascl:1710.003
- Eastman, J., Gaudi, B. S., & Agol, E. 2013, *PASP*, 125, 83
- Eastman, J. D., Rodriguez, J. E., Agol, E., et al. 2019, *arXiv e-prints*, arXiv:1907.09480
- Flewelling, H. A., Magnier, E. A., Chambers, K. C., et al. 2016, *ArXiv e-prints*, arXiv:1612.05243
- Frandsen, S., & Lindberg, B. 1999, in *Astrophysics with the NOT*, ed. H. Karttunen & V. Pirola, 71
- Gaia Collaboration, Brown, A. G. A., Vallenari, A., et al. 2018, *ArXiv e-prints*, arXiv:1804.09365
- Gardner, J. P., Mather, J. C., Clampin, M., et al. 2006, *SSRv*, 123, 485
- Gaudi, B. S., Seager, S., Mennesson, B., et al. 2018, *Nature Astronomy*, 2, 600
- Gelman, A., & Rubin, D. B. 1992, *Statistical Science*, 7, 457
- Gillon, M., Jehin, E., Magain, P., et al. 2011, in *European Physical Journal Web of Conferences*, Vol. 11, *European Physical Journal Web of Conferences*, 06002
- Høg, E., Fabricius, C., Makarov, V. V., et al. 2000, *A&A*, 355, L27
- Howell, S. B., Sobek, C., Haas, M., et al. 2014, *PASP*, 126, 398
- Huang, C. X., Burt, J., Vanderburg, A., et al. 2018, *ApJL*, 868, L39
- Irwin, J. M., Berta-Thompson, Z. K., Charbonneau, D., et al. 2015, in *Cambridge Workshop on Cool Stars, Stellar Systems, and the Sun*, Vol. 18, *18th Cambridge Workshop on Cool Stars, Stellar Systems, and the Sun*, ed. G. T. van Belle & H. C. Harris, 767–772
- Jenkins, J. M. 2002, *ApJ*, 575, 493
- Jenkins, J. M., Caldwell, D. A., Chandrasekaran, H., et al. 2010, *ApJL*, 713, L120
- Jenkins, J. M., Twicken, J. D., McCauliff, S., et al. 2016, in *Proc. SPIE*, Vol. 9913, *Software and Cyberinfrastructure for Astronomy IV*, 99133E
- Johnson, M. C., Dai, F., Justesen, A. B., et al. 2018, *MNRAS*, 481, 596
- Li, J., Tenenbaum, P., Twicken, J. D., et al. 2019, *PASP*, 131, 024506
- Lightkurve Collaboration, Cardoso, J. V. d. M. a., Hedges, C., et al. 2018, *Lightkurve: Kepler and TESS time series analysis in Python*, ascl:1812.013
- Livingston, J. H., Dai, F., Hirano, T., et al. 2018, *AJ*, 155, 115
- Livingston, J. H., Crossfield, I. J. M., Werner, M. W., et al. 2019, *AJ*, 157, 102
- Mayo, A. W., Vanderburg, A., Latham, D. W., et al. 2018, *AJ*, 155, 136
- Mayor, M., Pepe, F., Queloz, D., et al. 2003, *The Messenger*, 114, 20
- Oelkers, R. J., Rodriguez, J. E., Stassun, K. G., et al. 2018, *AJ*, 155, 39
- Paxton, B., Bildsten, L., Dotter, A., et al. 2011, *ApJS*, 192, 3
- Paxton, B., Cantiello, M., Arras, P., et al. 2013, *ApJS*, 208, 4
- Paxton, B., Marchant, P., Schwab, J., et al. 2015, *ApJS*, 220, 15
- Pepper, J., Kuhn, R. B., Siverd, R., James, D., & Stassun, K. 2012, *PASP*, 124, 230
- Pepper, J., Pogue, R. W., DePoy, D. L., et al. 2007, *PASP*, 119, 923
- Queloz, D., Mayor, M., Weber, L., et al. 2000, *A&A*, 354, 99
- Ricker, G. R., Winn, J. N., Vanderspek, R., et al. 2015, *Journal of Astronomical Telescopes, Instruments, and Systems*, 1, 014003
- Roberge, A., & Moustakas, L. A. 2018, *Nature Astronomy*, 2, 605
- Rodriguez, J. E., Quinn, S. N., Huang, C. X., et al. 2019, *AJ*, 157, 191
- Savitzky, A., & Golay, M. J. E. 1964, *Analytical Chemistry*, 36, 1627
- Schlafly, E. F., & Finkbeiner, D. P. 2011, *ApJ*, 737, 103
- Schlegel, D. J., Finkbeiner, D. P., & Davis, M. 1998, *ApJ*, 500, 525
- Shporer, A., Zhou, G., Fulton, B. J., et al. 2017, *AJ*, 154, 188
- Smith, A. M. S., Csizmadia, S., Gandolfi, D., et al. 2019, *AcA*, 69, 135

- Smith, J. C., Stumpe, M. C., Van Cleve, J. E., et al. 2012, *PASP*, 124, 1000
- Soto, M. G., Díaz, M. R., Jenkins, J. S., et al. 2018, *MNRAS*, 478, 5356
- Stassun, K. G., & Torres, G. 2018, *ApJ*, 862, 61
- Stumpe, M. C., Smith, J. C., Catanzarite, J. H., et al. 2014, *PASP*, 126, 100
- Stumpe, M. C., Smith, J. C., Van Cleve, J. E., et al. 2012, *PASP*, 124, 985
- Szentgyorgyi, A., Baldwin, D., Barnes, S., et al. 2016, Society of Photo-Optical Instrumentation Engineers (SPIE) Conference Series, Vol. 9908, The GMT-Consortium Large Earth Finder (G-CLEF): an optical Echelle spectrograph for the Giant Magellan Telescope (GMT), 990822
- Thompson, S. E., Coughlin, J. L., Hoffman, K., et al. 2018, *ApJS*, 235, 38
- Twicken, J. D., Catanzarite, J. H., Clarke, B. D., et al. 2018, *PASP*, 130, 064502
- Vanderburg, A., & Johnson, J. A. 2014, *PASP*, 126, 948
- Vanderburg, A., Montet, B. T., Johnson, J. A., et al. 2015, *The Astrophysical Journal*, 800, 59
- Vanderburg, A., Becker, J. C., Kristiansen, M. H., et al. 2016a, *ApJL*, 827, L10
- Vanderburg, A., Latham, D. W., Buchhave, L. A., et al. 2016b, *ApJS*, 222, 14
- Vanderspek, R., Huang, C. X., Vanderburg, A., et al. 2019, *ApJL*, 871, L24
- Virtanen, P., Gommers, R., Oliphant, T. E., et al. 2020, *Nature Methods*, 17, 261
- Vogt, S. S., Allen, S. L., Bigelow, B. C., et al. 1994, in *Proc. SPIE*, Vol. 2198, Instrumentation in Astronomy VIII, ed. D. L. Crawford & E. R. Craine, 362
- Wheatley, P. J., West, R. G., Goad, M. R., et al. 2018, *MNRAS*, 475, 4476
- White, T. R., Huber, D., Mann, A. W., et al. 2018, *MNRAS*, 477, 4403
- Zacharias, N., Finch, C., & Frouard, J. 2017, *VizieR Online Data Catalog*, 1340